Reduced trap density and mitigating the interfacial losses by placement of 2D dichalcogenide material at perovskite/HTM interface in a dopant free perovskite solar cells

Naveen Harindu Hemasiri[1], Samrana Kazim[1,2] and Shahzada Ahmad[1,2]*

[1]BCMaterials, Basque Center for Materials, Applications and Nanostructures, Bld. Martina Casiano, UPV/EHU Science Park, Barrio Sarriena s/n, 48940 Leioa, Spain

Tel: +34 946128811 Email:shahzada.ahmad@bcmaterials.net

[2]IKERBASQUE, Basque Foundation for Science, Bilbao, 48013, Spain

Abstract

Solution-processed photovoltaics employing perovskite as light harvester are the next generation future energy source owing to its low manufacturing cost and potential to achieve high power conversion efficiency. Significant emphasis has been laid on the performance-related investigations, however the long-term instability under operational conditions and device reproducibility obstruct its potential commercial endeavour. Herein, by tweaking the energy level alignment between the hole-transport layer and perovskite, by the placement of a thin 2D-MoS_2 interlayer, we demonstrate suppressed interfacial charge accumulation, fast charge extraction, and subsequently improved photovoltaic performances. Notably, with the usage of a dopant free hole transport materials, a power conversion efficiency of 18.54% with significantly upgraded open circuit voltage (V_{oc}) and FF was recorded. The stability measurement shows that the resulting 2D-MoS_2 supported dopant-free hole selective layers exhibit notable moisture stability under ambient conditions. Our study put forward the profound experimental understanding of 2D-transition metal dichalcogenides as an agent to engineering the interface, enlightening the power conversion efficiency and lifetime of the perovskite solar cells.

Keywords: 2D MoS_2, interface engineering, dopant-free HTM, improved stability, open circuit voltage

1. Introduction

In thin film photovoltaics (PV), hybrid halide perovskite solar cells (PSCs) have shown astonishing development with an unprecedented rise in power conversion efficiency (PCE) from 3.8 % to 25.2 % within a decade, signalling as cost-effective renewable PV technology.[1,2] Despite the tremendous progress in the PCE of PSCs, the issue of intrinsic device stability, mainly induced by light irradiation, ionic migration, moisture corrosion, and oxygen infiltration under prolong operational conditions hinders their potential commercialization.[3] Further, hysteresis in current density-voltage (*J*-*V*) curve in devices due to charge traps of the active layer needs to be rationally addressed for the unification of device performance.[3,4]

The open circuit voltage (V_{oc}) of the devices can easily diminish with a lack of charge-density build up and pulling down the quasi-Fermi level splitting due to non-radiative carrier recombination centers that arises from electronic trap states through crystallographic defects and higher-dimensional defects such as grain boundaries.[5,6] Furthermore, these defect sites facilitate nucleating sites for degradation, which annihilate the operation lifetime of the solar cells.[5,7] Even though the numerous endeavours have been directed towards the development of materials to passivate specific defects, most of the additives militate against the PCE enhancement.[6,8] On the other hand, photo-generated carriers should be extracted efficiently to avoid the generation of new defects as the active layer i.e. perovskite associated with the low defect formation energy.[6] The extrinsic environmental condition, i.e., light intensity, electric field, and temperature during device operation can promote the natal local defects towards the degradation of the active layer, thus it is paramount to extract the untrapped and detrapped carriers promptly to militate charge accumulation and recombination.[6,9,10]

The apparent *J*-*V* hysteresis and poor stability originate not only from the defective active layer and disordered charge transport, but also from perovskite/charge transport layer (CTL) interfaces, and charge extracting materials.[4,11,12] The interface between the hole transport material (HTM) and the perovskite remains the vulnerable part in the device for stability as trapped charges at the interface between perovskite and charge extraction layer are responsible for the irreversible degradation caused by moisture.[11,12] In particularly, commonly used organic HTMs, for example, poly(3,4-ethylenedioxythiophene), *2,2′,7,7′*-tetrakis(*N*,*N*-di-4-methoxyphenylamine)-9,9′-spirobifluorene (Spiro-OMeTAD), or poly(triarylamine) (PTAA), shows insufficient charge carrier mobility in their pristine form, and doping is a prerequisite, hygroscopic materials are mostly used as dopant to obtain excellent PV properties.[3,13,14] The usage of such dopants further accelerate the degradation of the HTM layer and subsequently

the perovskite layer.[3,13,14] To overcome such challenges, strategies have been pointed to improve the stability of the PSCs including rational designing of transport layer, interface modifications and eliminating the moisture infiltration into the active layer by coating of polymers, hydrophobic materials and carbon-based materials, most of these approaches is a trade of with device PV performance.

In the context of optoelectronics, two-dimensional (2D) transition metal dichalcogenides (TMDs), especially MoS_2, owing to its unique optoelectronic properties including fast transport of the charges in the vertical direction and chemical inertness with high electron mobility and fewer traps make it as a potential candidate to replace conventional CTLs.[15] Kim et al. firstly introduced chemical vapour deposition grown MoS_2 in inverted PSCs followed by Huang et al. report on solution-processed MoS_2 as CTL to substitute PEDOT:PSS and measured 14% PCE.[16] Further, Li *et al*. noted that the percentage of metallic octahedral 1T phase decreases with the post-heating due to phase transformation from 1T to 2H, and the reduction of 1T phase in 2D-MoS_2 influence the PV performances to a large extent. The authors reported enhanced PCE with 1T-rich 2D-MoS_2 as compared to the 1T-poor 2D-MoS_2 as HTL in *p-i-n* type PSCs from 7.64 to 13.62%.[16] Recently, Singh et al. demonstrated 2D-MoS_2 as ETL in a PSCs and measured 13% PCE, indicating the bottleneck of employing 2D-MoS_2 as individual CTL is not competitive in terms of PCE due to interfacial energy loss via deep ionization levels associated with the 2D-TMDs, despite the excellent stability.[17,18] Interface engineering utilizing 2D materials has demonstrated promising results in the terms of stability and PCE enhancement. Kakavelakis and co-workers has employed solution based MoS_2 as a hole extraction interlayer with PTAA in inverted PSCs with improved stability and PCE.[13] However, the elucidation of its functioning and operating mechanisms of the 2D-MoS_2 as interfacial layer in PSCs are limited and obscure.

In the present work, we experimentally demonstrate the use of intercalated Li^+ based solution-processable 2D-MoS_2 flakes as hole extraction interlayer in *n-i-p* type PSCs using triple-cation perovskite [$Cs_{0.1}FAPbI_{3(0.81)}MAPbBr_{3(0.09)}$] and dopant-free PTAA to improve optoelectronic properties and operation stability. The fabricated device gave an improved PCE of 18.54% and lifetime as compared to the controlled device without MoS_2 interlayer (15.05% PCE). The improvement is ascribed to the efficient hole extraction with the stabilization of the perovskite/HTM interface, band alignment and mitigating the degradation in the active layer.

2. Results and Discussion

The stable 2D-MoS_2 sheets consist of a mixture of two distinct phases; prismatic 2H and octahedral 1T in isopropanol (IPA) were achieved from bulk MoS_2 by Li^+ intercalation assisted

liquid-phase exfoliation (LPE). This enables to exfoliate TMDs into a few layers or in some cases a monolayer (detailed in experimental section). The buried van der Waals forces in between MoS_2 is attributed to the hydrodynamic shear-force associated with the ultrasonication steps in the LPE process.

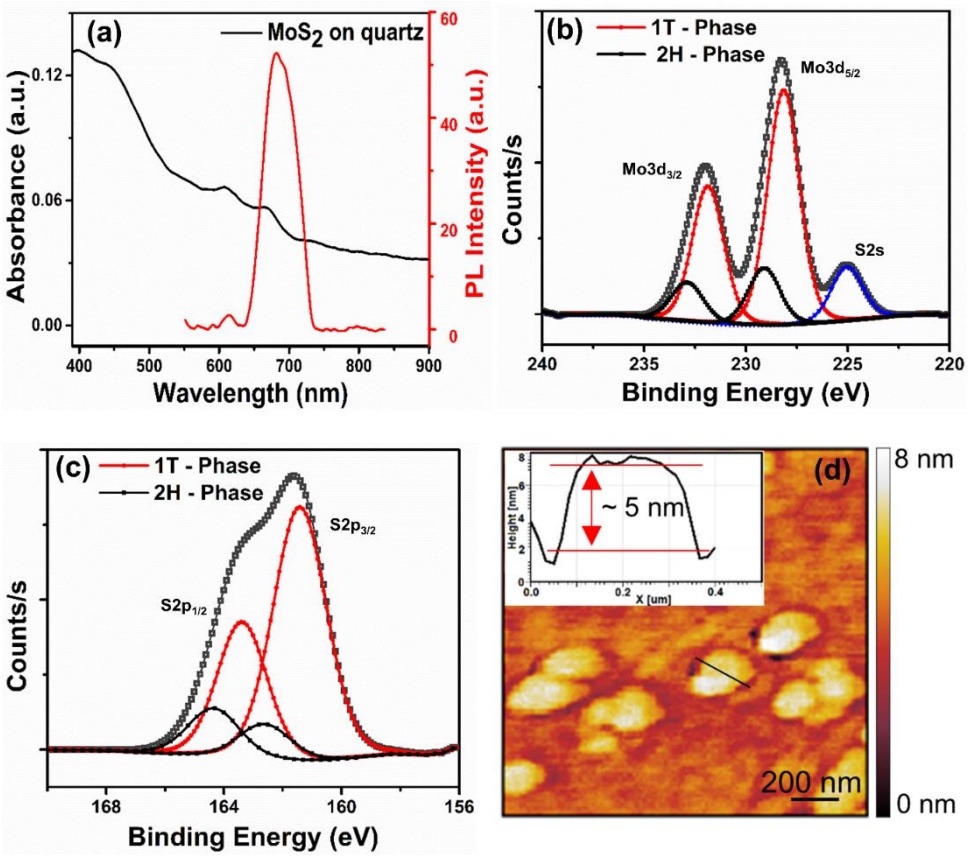

Figure 1. (a) UV-Vis absorbance and photoluminescence spectra of spin coated 2D-MoS_2 on quartz substrate. XPS narrow spectrum of (b) Mo3d and (c) S2p of spin coated MoS_2 thin film and (d) topography of drop casted MoS_2 thin film on Si substrate, inset shows the thickness profile.

Figure 1a depicts the UV-Vis absorption spectra of the spin coated 2D-MoS_2 on quartz substrate. The two shoulder peaks, located at c.a 675 and 625 show direct excitonic transitions between the split valance band and the minima of the conduction band at the K-point of the Brillouin zone of layered MoS_2 structure due to the formation of 1T-phase.[5,13,19,20] Similar absorption features were noted from the 2D-MoS_2 solution in isopropanol (Figure S1). The photoluminescence (PL) peaks at about 680 and 630 nm correspond to the upper (A, 1.82 eV) and lower (B, 1.96 eV) direct-gap optical transitions respectively (inset of Figure 1a).[21-23] We found that the as-prepared 2D-MoS_2 is predominantly in the metallic 1T phase, achieving 78.3%, which was quantitatively investigated from the X-ray photoelectron spectroscopy

(XPS) measurements (Figure 1 b and c). Two identical deconvoluted peaks appeared at 231.9 and 228.2 eV are assigned to the $Mo3d_{3/2}$ and $Mo3d_{5/2}$ of 1T phase respectively. The $Mo3d_{3/2}$ and $Mo3d_{5/2}$ two peaks relevant to 1T phase show 1 and 0.9 eV difference towards the lower binding energy with respect to its 2H phase respectively. The absence of peaks at 236 and 233 eV suggests the synthesized 2D-MoS_2 is free of Mo oxidized phases derived through Li^+ assisted liquid phase exfoliation process.[24] The associated 1T phase corresponding to the binding energy of $S2p_{1/2}$ and $S2p_{3/2}$ reached to 163.41 and 161.41 eV respectively (Figure 1c). The influence of various phases of 2D-MoS_2 on the PV performance was elucidated, 2H-predominant 2D-MoS_2 was synthesized through liquid exfoliation with the absence of Li^+ intercalation.[25] The contribution of the 2H phase in synthesized 2D-MoS_2 via the aforementioned method was 81.69% and we noted 232.09 and 229.29 eV binding energies corresponding to $Mo3d_{3/2}$ and $Mo3d_{5/2}$ of 2H phase respectively (Figure S2).

A thermodynamically unstable 1T-MoS_2 where Mo atoms arranged in an octahedral manner, consisting of better conduction properties than its counterpart (2H-MoS_2) can undergo phase transformation back to the initial 2H phase under moderate temperature, thus, we managed to avoid the post-heating process of the MoS_2 layer during device fabrication.[16,18,26,27] Li *et al.* investigated the charge carrier extraction using PL spectroscopy, 1T rich MoS_2 shows excellent charge carrier extraction from perovskite due to high conductivity associated with 1T phase as compared to 2H phase, and resulted in improved PV properties.[16] The thickness of the MoS_2 flakes was recorded by atomic force microscopy (AFM) imaging (Figure 1d). The inset represents thickness profile and the thickness of the flakes was 5 nm. The large scan area of AFM topography image further suggest the thickness of 2D-MoS_2 (Figure S3). Transmission electron microscopy experiments were carried out to further investigate the as-prepared 2D-MoS_2, which confirmed the existence of 2D layered structure of the exfoliated MoS_2 having the average flakes size of 300 nm (Figure S4). Further, we noted the as prepared 2D-MoS_2 makes stable dispersion in isopropanol (Figure S1). For electron selective layer, stable water-soluble colloidal SnO_2-QD was synthesized and used as n-type selective contact atop of compact thin blocking layer to improve the hole-blocking properties associated with SnO_2.[28,29] The scanning electron microscopy (SEM) images of SnO_2-QD layer on compact TiO_2 (**Figure 2**b) reveals the formation of uniform, continuous and pinholes free SnO_2 layer. The smooth layer facilitates effective electron transportation and build favourable interface for high quality perovskite deposition. Figure 2c depicts the perovskite film grown on SnO_2-QDs exhibits average grain size of 315 nm.

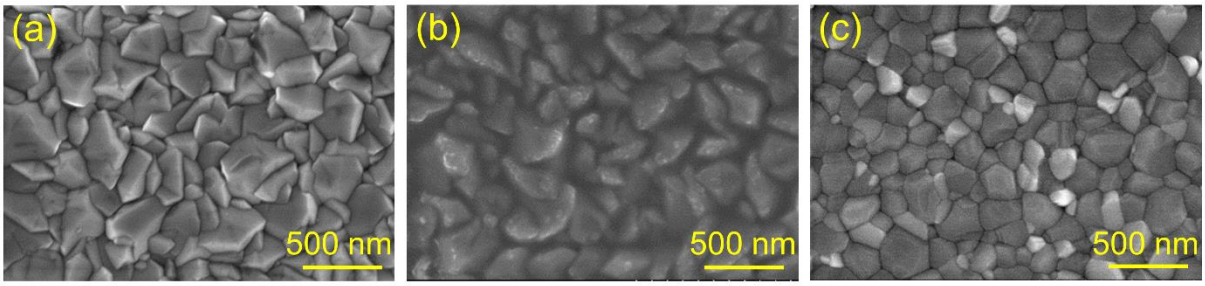

Figure 2. SEM images of (a) FTO substrate, (b) SnO_2-QD layer on c-TiO_2/FTO and (c) the triple cation perovskite grown on SnO_2-QD/c-TiO_2/FTO.

The synthesized MoS_2 was placed as an interfacial layer into a PSCs in a device architecture of FTO/c-TiO_2/SnO_2 QD/$Cs_{0.1}FAPbI_{3(0.81)}MAPbBr_{3(0.09))}$/$MoS_2$/PTAA/Au (**Figure 3**a) and a typical cross sectional SEM image is illustrated in Fig. S6 (Supporting Information). For the ease of terminology hereafter, the triple cation perovskite will be termed as CsFAMA. SnO_2 based electron selective layer together with c-TiO_2 provides enhanced hole-blocking ability than only SnO_2. This was used to avoid any direct contact with the bottom charge collector and eliminate possible recombination path, which in turn will improve the PCE. The energy level alignment of the materials used for the PSC fabrication, with the 2D-MoS_2, is represented in Figure 3b, where the valence energy level (E_v) of 2D-MoS_2 minimizes the energetic mismatch between the CsFAMA and pristine PTAA. Figure 3c depicts the *J-V* characteristics under AM 1.5G illumination (100 mW cm^{-2}) of control and MoS_2 based devices, and the PV parameters are represented in **Table 1**. The control devices yielded an average PCE of 15.05% with a short-circuit current density (J_{sc}) of 22.70 $mAcm^{-2}$, an open-circuit voltage (V_{oc}) of 887.7 mV and a fill factor (FF) of 74.64%. Notably, the devices fabricated by placing MoS_2 as an interfacial layer showed significant improvement and gave an average PCE >18%, mainly due to the increased of ~164mV in V_{oc} and ~ 5% in FF. The increment in V_{oc} was obtained by stabilizing the HOMO level to minimize the mismatch between the absorber and HTM layer to just 0.31 eV and increase in carrier concentration, which increases the FF. The device incorporated with 2D-MoS_2 interface layer gave 18.54% PCE that is a significant increment of 23.2% as compared to the control device, which measured 15.05% PCE under similar condition. To note the accuracy of the obtained J_{sc} from *J-V measurements*, we performed the incident photon-to-current efficiency (IPCE) measurements (Figure 3d). The integrated J_{sc} values from the IPCE spectra are 22.27 and 21.72 $mAcm^{-2}$ for the control and modified device respectively, and the values are in well agreement with J_{sc} obtained from *J-V* measurements. The standard deviation of the PV parameters are tabulated in Table S1.

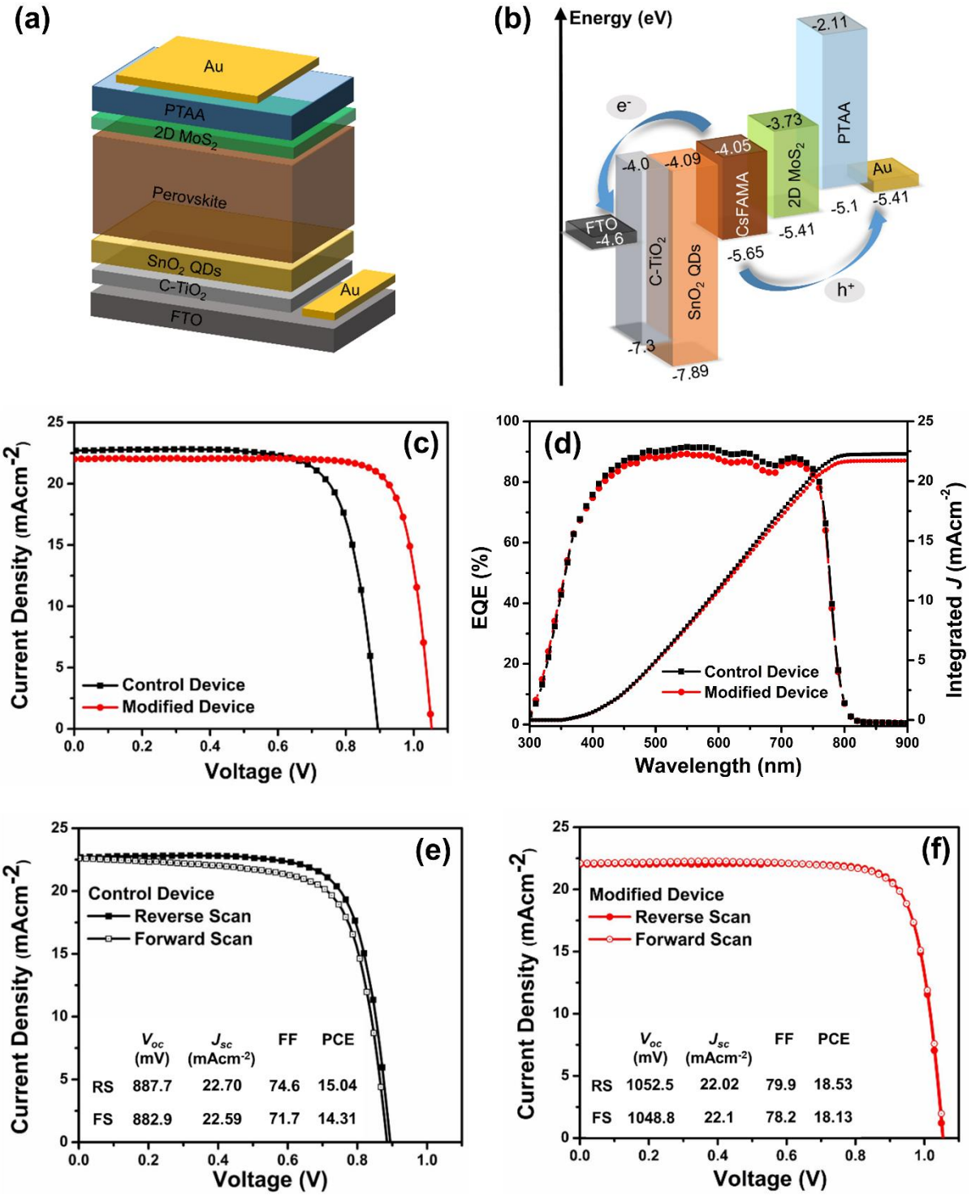

Figure 3. (a) Device architecture, (b) energy level diagram of the fabricated PSCs, (c) *J-V* curves of the champion CsFAMA devices (control and modified) under simulated AM 1.5G illumination, (d) corresponding IPCE and integrated J_{sc} of champion devices and *J-V* hysteresis curve of forward and reverse scans of (e) control and (f) of modified device.

Table 1. PV parameters of the fabricated PSCs with and without 2D-MoS_2 interface layer

Device	Direction	V_{oc} (mV)	J_{sc} (mAcm^2)	FF (%)	PCE (%)	R_s (Ω cm^2)	R_{sh} (kΩ cm^2)	HI
Control	RS	887.7	22.70	74.64	15.04	3.21	3.85	0.050
	FS	882.9	22.59	71.75	14.31	3.91	0.99	
1T-Modified MoS_2)	RS	1052.5	22.02	79.96	18.54	2.85	7.09	0.001
	FS	1048.9	22.10	78.21	18.13	3.11	5.63	

[a]R_s and R_{sh} of PSCs were estimated by slope of the *J-V* curves near V_{oc} and J_{sc}, respectively.

The enhanced V_{oc} of the modified device can be explained by the valence band maximum (VBM) of 2D-MoS_2 (-5.4 eV), which reduced the wide energy barrier and mismatching between the valence band energy level (E_v = -5.65 eV) of CsFAMA and the HOMO level of pristine PTAA (-5.1 eV), facilitating smooth hole extraction from perovskite to the HTL.[12,24] In particular, the 2-dimensional nature of MoS_2 opens the wide optical bandgap compared to its bulk form from 1.2 eV − 1.8 eV, raising the conduction band of MoS_2 atop of the conduction band minimum (CBM) of CsFAMA, subsequently providing electron-blocking properties at perovskite/HTL interface (Figure S5).[24,30-32] As depicted in Table 1, the control device showed higher series resistance (R_s) of 3.21 Ω cm^2, whereas the MoS_2 interlayer based device gave notably reduced R_s of 2.85 Ω cm^2, and subsequently improved FF was obtained. Apart from R_s, shunt resistance (R_{sh}) also affects the FF.[33] The presence of 2D-MoS_2 with effective electron blocking properties is responsible for the high R_{sh} associated with the modified device (7.09 kΩ cm^2 for RS) compared to the control device (3.85 kΩ cm^2 for RS). The excellent hole extraction behaviour in conjugation with electron-blocking properties of 2D-MoS_2 synergistically suppress the interfacial recombination losses, providing effective surface passivation to the active layer. Arguably, we can conclude that introducing 2D-MoS_2 as an interfacial layer in between perovskite/HTL, the PV parameters have been noteworthy improved. The hysteresis behaviour was measured by scanning *J-V* curves in reverse and forward direction (Figure 3e and f), where the hysteresis index (HI) is acquired to quantify the degree of hysteresis using the following equation;[4,34]

$$\mathrm{HI} = \frac{J_{RS\,(0.8\,Voc)} - J_{FS(0.8Voc)}}{J_{RS(0.8Voc)}} \quad (1)$$

where $J_{RS(0.8Voc)}$ and $J_{FS(0.8Voc)}$ represent the J_{SC} at 80% of V_{OC} of the reverse and forward scan respectively. The calculated HI of the device with 2D-MoS_2 shows alleviated photocurrent hysteresis (0.001 of HI) compared to the control device.

Apparently, the PSCs with 2H-predominant 2D-MoS_2 as an interfacial layer also gave improved PV performance than of control device without any interfacial layer, the device yielded a PCE of 17.34% with a short-circuit current density (J_{sc}) of 22.22 $mAcm^{-2}$, V_{oc} of 1018.9 mV and FF of 76.61% under AM 1.5G illumination (100 $mWcm^{-2}$). The *J-V* hysteresis curve and corresponding IPCE are presented in Figure S8 and Table S3. However, we noted limited improvement in device performance as compared to the PSCs with 1T-predominant 2D-MoS_2. We ascribed this to the higher conductivity value (10^7 times higher) associated with 1T-MoS_2 as compared to 2H-MoS_2, which influences PV performances between 1T-predominant and 2H-predominant 2D-MoS_2 when used as an interfacial layer in PSCs.[35,16] Table 2 shows comparative study of the state of the art value together with our current work.

Table 2. Interfacial engineering for improving the performance and stability of PSCs

Type	Device structure	PCE (%)	Stability	Reference
n-i-p	FTO/$cTiO_2$/SnO_2QDs/CsFAMA/2DMoS_2/PTAA[a]/Au	18.29	80%(45h)[x]	Current study
p-i-n	ITO/PTAA[a]/$(BA)_2(MA)_3Pb_4I_{13}$/C60/BCP/Ag	17.26	96%(2000h)[y]	36, 37
n-i-p	FTO/SnO_2/$(FAPbI_3)_{1-x}(MAPbBr_3)_x$/PTAA[b]/Au	21.21	86%(1480h)[x]	38, 39
n-i-p	FTO/$cTiO_2$/$MAPbI_3$/Spiro-OMeTAD/MoO_3/Ag	19.41	80%(720h)[x]	38, 40
p-i-n	ITO/PTAA[a]/2DMoS_2/MAPI/PCBM/PEN/Al	16.42	80%(6h)[x]	13
n-i-p	FTO/$cTiO_2$/$mTiO_2$/MAPI/PTAA[a]/Au	12.73	N/A	4
p-i-n	ITO/PEDOT:PSS/MoS_2/MAPI/PCBM/Bphen/Ag	16.32	N/A	41
n-i-p	FTO/MoS_2/$MAPbI_3$/Spiro-OMeTAD/Au	13.14	N/A	15
n-i-p	FTO/$cTiO_2$+G/$mTiO_2$+G/perovskite/Spiro-OMeTAD/MoS_2 or f-MoS_2/Au	15.3	80% (65 ^oC,370h)	42

[a]un-doped, [b]doped, [x]un-encapsulated and [y]encapsulated or un-encapsulated in Ar or N_2 atmosphere.

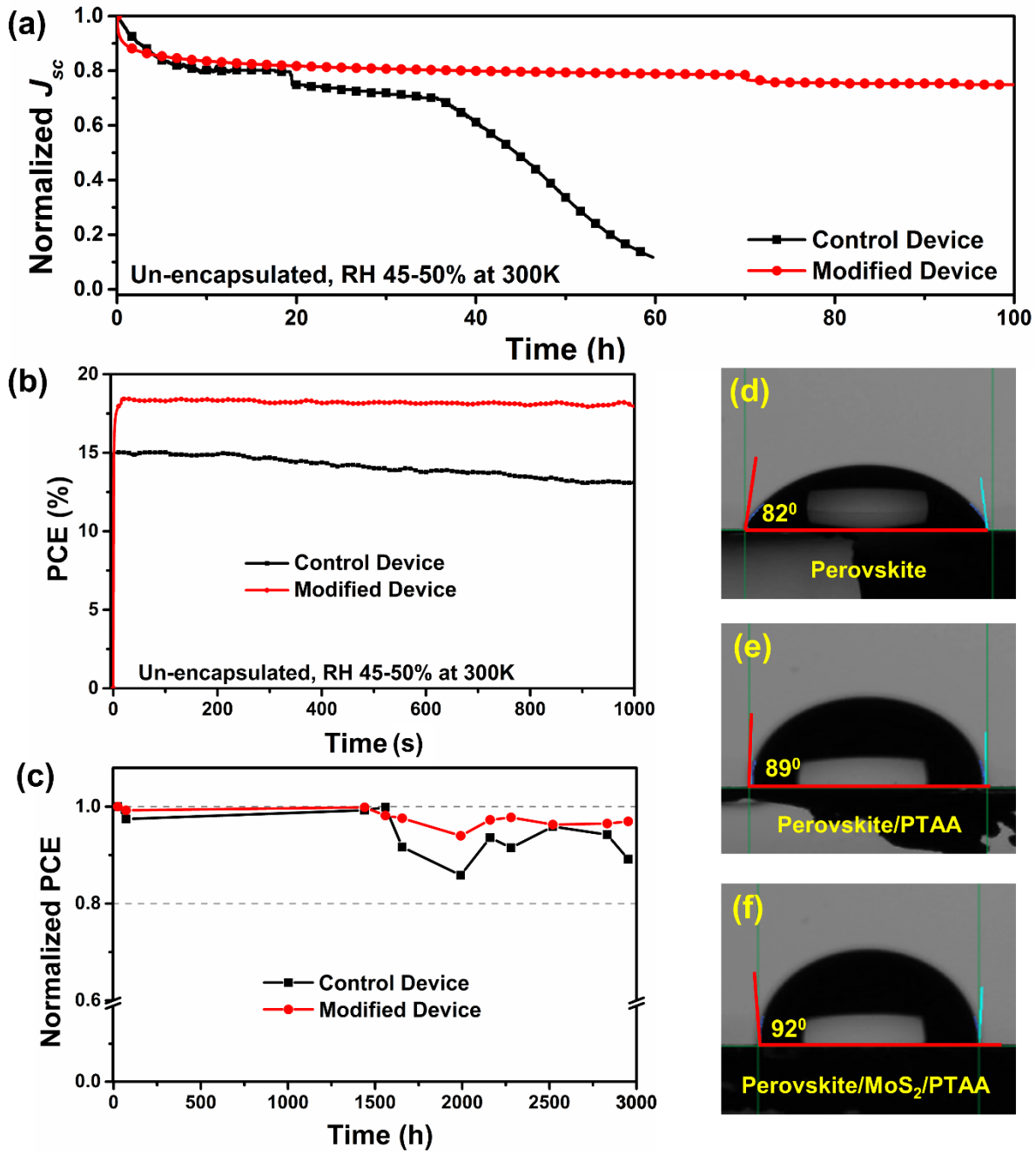

Figure 4. (a) Normalized J_{sc} for 100 h of continuous MPP tracking of the control and modified devices under constant 1 sun illumination at ambient atmosphere, (b) the stabilized power output of the devices under constant 1 sun illumination at ambient atmosphere, (c) normalized PCE with the storage time of control and modified devices in ambient atmosphere, and contact angle measurements for (d) CsFAMA, (e) CsFAMA/PTAA and (f) CsFAMA/2D-MoS_2/PTAA.

2D-MoS_2 based PSCs gave superior PV properties, to ascertain the interfacial engineering might compromise the operational stability of devices, we conducted maximum power point tracking (MPPT) of the un-encapsulated devices under constant 1 sun illumination and 45-50 % humidity at room temperature (**Figure 4**a). The control device drastically lost 20% of its initial photocurrent value after 22 h of continuous testing, while the modified device with 2D-MoS_2 maintained 80% of its initial photocurrent for around 45h of continuous operation. Further, the modified device showed 75% of its initial photocurrent after 100h continuous operation conditions. We probed the long-term stability of PSCs in storage condition where the un-encapsulated PSCs were stored in a dry box with relative humidity maintained at 45-50 % at room temperature (Figure 4b). The modified devices maintained 96% of its initial PCE for 2952 h while the control devices showed 89% of its initial PCE during this time. The plausible reason for this was improved surface properties obtained by the placement of MoS_2, which will act as barrier for moisture diffusion inside of the perovskite layer. Surface topography images revealed that the RMS roughness of films was reduced from 15.39 to 12.33 nm by the placement of 2D-MoS_2 (Figure S10). Arguably, this induced surface smoothness on the perovskite layer facilitates uniform distribution of the PTAA atop of it, and we noted, RMS roughness of the PTAA layer was reduced from 4.14 to 1.61 nm with the placement of interfacial layer. The humid environment negatively influences the stability of the perovskite active layers and form perovskite hydrates easily, this initiates the decomposition and device degradation.[43] The hindering of moisture penetration to the active layer mitigates the degradation process and will subsequently extend the lifetime of the devices. The hydrophobic nature associated with 2D-MoS_2 put forward a strong affinity for water repulsion and moisture protection to the active layer.[44-49] The water contact angle value is higher for the samples with PTAA deposited on perovskite with the presence of MoS_2 as interfacial layers, as compared to the reference device (Figure 4d,e). Pointing towards the attained hydrophobicity associated with the modified devices that can mitigate the water penetration into the active perovskite layer.

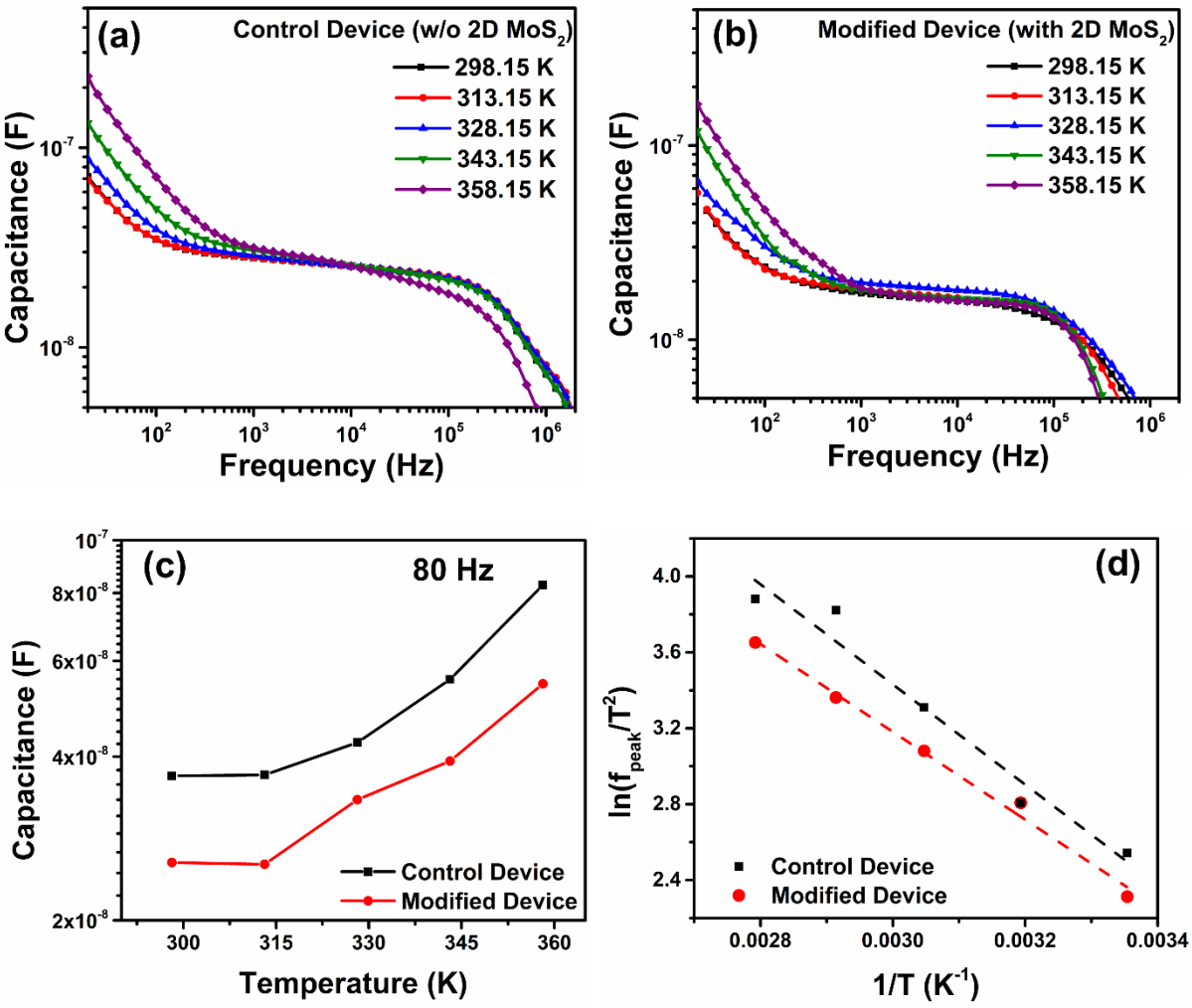

Figure 5. Capacitance-frequency-temperature spectra obtained from (a) control device, (b) with MoS_2, (c) temperature dependence low frequency capacitance of control and modified devices and (d) Arrhenius plot of $\ln(f_{peak}/T^2)$ versus 1/T for control and modified devices, extracted from –fdC/df versus f spectra.

Both electronic and ionic type charge carriers in perovskite play determining role in the overall performance, however under electric field ionic defects can drift and accumulate at the interface due to poor extraction and mobility of charge transporting carriers, resulting capacitance build up in the device.[50-52] To identify the factors accountable for the increment in PCE of fabricated PSCs, we studied the charge accumulation behaviour of the devices with and without the 2D-MoS_2 interfacial layer through capacitance-frequency measurement at variable temperatures under dark conditions. **Figure 5**a and b enumerate the variation of capacitance (*C*) as a function of frequency (*f*) of devices at different temperatures. Three identical features were observed according to the three distinct regions of frequency: low (LF,

20 Hz-1 kHz), intermediate (IF, 1-100 kHz), and high (HF, 100 kHz-2 MHz) in both graphs. At IF region, a constant capacitance is identified, assigned to dielectric relaxation in the active layer which is mainly determined by the geometrical capacitance per unit area (C_g). This varies with the dielectric constant (ε), the geometrical layer thickness (L) of the perovskite layer, and vacuum permittivity (ε_0), [$C_g = \varepsilon\varepsilon_0/L$].[52,53] The constant value of capacitance at IF with an increase in temperature of both devices suggests, stable geometrical capacitance associated with the perovskite layer. Toward low frequencies, thermally-activated capacitance improvement was deducted which was ascribed to the charge accumulation at the interface and interfacial properties rather than bulk.[54-56] However, the control device showed much higher capacitance than the device with 2D-MoS_2 interface layer in the LF region, suggesting that the charge carrier build-up at the interface is higher for control device. Owing to the presence of 2D-MoS_2, the trapped-carriers located at the interface gain sufficient thermal energy to depart from the interface and migrate towards the bulk perovskite, consequently the drop of the thermal-activated capacitance increment at the LF of the modified device occurs.[54,56,57] Arguably, the presence of 2D-MoS_2 as an interfacial layer avoid charge accumulation at the perovskite/HTL interface and capacitance build up in the PSCs under DC bias voltage. The capacitance drop at the HF region correlates to the effect of the series resistance caused by conductive contact layer.[56]

Figure 5c depicts the capacitance measured at around 80 Hz as a function of the temperature, slight increment in thermally activated capacitance in both devices can be deducted, while comparatively higher capacitance value identified for control device at variable temperature range due to high charge accumulation at the PSK/PTAA interface through poor carrier extraction and migration. Further, the unbalance charge extraction and transport associated with the pristine PTAA allows the capacitance build-up at perovskite/HTL interface.[57] To elucidate the role of interfacial layer on the distribution of trap density in the CsFAMA layer, we determined the frequency of peak (f_{peak}) emission rate of electrons from a trap state located below E_T to E_c (conduction band edge) and activation energy for the devices. The f_{peak} was extracted from the derivative of capacitance spectra in the form of –fdC/df as a function of f (Figure S7a and b). The activation energy E_a was calculated from the Arrhenius plot (Figure 5d), ln f_{peak}/T^2 vs. 1/T and the following equation;[57-59]

$$\ln\frac{e_n}{T^2} = \ln\frac{v_o}{T^2} - \frac{E_a}{K_B T} \quad (2)$$

where e_n is the emission rate of electrons from a trap state, v_0 is attempt-to-escape frequency (ATEF), E_a is the activation energy, K_B is the Boltzmann constant, and T is the temperature. The trap energy for control and MoS_2 based devices are 227 and 199 meV respectively, indicating that charge transportation is hindered in the control device.[58,60,61] The intercepts of Arrhenius plot yields corresponding ATEF (v_0) of 7.58×10^9 Hz for the control device that is much higher than of modified device showing v_0 of 2.22×10^9 Hz and **Table 2** summarizes the extracted parameter.

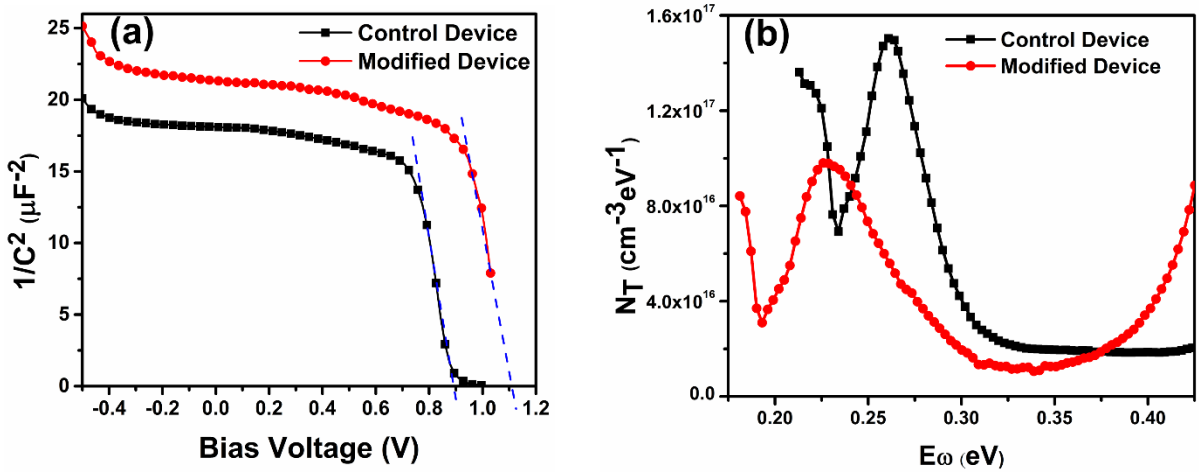

Figure 6. (a) Mott-Schottky analysis at 10 kHz and (b) trap density (N_T) of control and modified devices measured at 300 K.

The trap density distribution (N_T), built-in-potential (V_{bi}), and depletion layer width (W) at perovskite/HTL interface were determined by using Mott-Schottky analysis along with the thermal admittance spectroscopy (TAS). **Figure 6**a depicts the Mott-Schottky plot of devices at 10 kHz, the plot yields a straight region from which V_{bi} was extracted from the intercept on the bias axis and the doping density of immobile ions (N) at depletion region was determined from the slope. The aforementioned parameters are related to the capacitance (C) as follows;[62-64]

$$\frac{1}{C^2} = \frac{2}{\varepsilon\varepsilon_0 A^2 qN}\left[V - V_{bi} - \frac{K_b T}{q}\right] \quad (3)$$

where ε is relative dielectric constant of perovskite (taken as the value of 32 from a previous report), ε_0 is permittivity of free space and A is active interfacial area.[65] Here K_b, T, and q

represent Boltzmann´s constant, the absolute temperature, and elementary charge respectively. The built-in-potential for the modified device with 2D-MoS_2 interfacial layer was found to be increased to 1137.6 mV from 895.5 mV for the control device without the interface layer. Consequently, the depletion width ($W=\sqrt{\frac{2\varepsilon\varepsilon_0 V_{bi}}{qN}}$) of the active layer was increased from 131.69 nm for control device to 134.43 nm for the device with 2D MoS_2 interface layer. The enhanced depletion region assists in the proper charge separation and annihilates the recombination, and thus contributes to the increases in the PCE. The energetic profile of trap density of state (t_{DOS}) was calculated from the following equations;[66,67]

$$N_T(E_f) = -\frac{V_{bi}}{qWK_bT}\left[f\frac{dc}{df}\right] \quad (4)$$

$$E_f = K_bTln\left[\frac{v_0}{f}\right] \quad (5)$$

The trap density (N_T) profile as shown in Figure 6b indicates that the incorporation of 2D-MoS_2 as an interfacial layer significantly reduced the overall trap density of state in the perovskite. The distribution of trap density of state (t_{DOS}) in control device exhibit a peak value of 1.5×10^{-17} $cm^{-3}eV^{-1}$ situated at 0.26 eV which shifts to the lower energy at 0.226 eV with reduce value of 9.8×10^{-16} $cm^{-3}eV^{-1}$ in case of MoS_2 based device.

The remarkable decrease of the t_{DOS} was consistent with the decreased photocurrent hysteresis, indicating the effective passivation of charge traps in CsFAMA by 2D-MoS_2. The suppressed trap density in the band gap of the perovskite in combination with 2D-MoS_2 efficiently extracts the photo-generated carriers to mitigate the interfacial charge recombination. We speculate this reduced trap density as a result of possible electron blocking effect from 2D-MoS_2 (Fig. S5), suggesting the reduced or eventually eliminating the PV hysteresis in the devices.

Table 2. Electrical parameters calculated for control and modified devices from thermal admittance spectroscopy and Mott-Schottky plot at 300 K.

Parameters	**Control**	**With MoS_2**
Activation energy $\boldsymbol{E_a}$ (meV)	227	199
ATEF v_0 (Hz)	7.58×10^9	2.22×10^9
Built-in-potential $\boldsymbol{V_{bi}}$ (V)	0.8955	1.1376
Depletion layer thickness (nm)	131.69	134.43
Trap density at Peak, $\boldsymbol{t_{DOS}}$ $(eVcm^3)^{-1}$	1.50×10^{17}	9.8×10^{16}

energy at peak (E_ω) t_{DOS} (eV)	0.261	0.226

3. Conclusions

To summarize, we have presented the role of 2D-MoS_2 as an interfacial layer in perovskite solar cells, in improving the opto-electrical properties by minimizing energetic mismatch and suppressing trap density in the perovskite layers. In a triple cation (CsFAMA) based perovskite environment, we noted 2D-MoS_2 interfacial layer reduces the energy required for detrapping the trapped-charges, by providing prompt extraction of photo-generated charges while mitigating the interfacial charge recombination. Our strategy based on interface engineering enables us to demonstrate dopant-free *n-i-p* structured devices with 18.54% power conversion efficiency along with enhanced long-term operational stability. The present work put forward the placement of 2D-interlayer in conjugation with dopant free hole transport layer to amplify the device photovoltaic performance and stability, which is paramount for the success of perovskite solar cells.

4. Experimental Section

Materials: Molybdenum (iv) sulfide (MoS_2, 99% metal basis, -325 mesh powder), tin (ii) chloride dehydrate ($SnCl_2.2H_2O$, 98%), and thiourea (CH_4N_2S, 99%) were procured from Alfa Aesar while butyl lithium (1.6M, hexane) from Sigma-Aldrich. The chemicals for perovskite were purchased from Dyesol except PbI_2 and CsI_2 that were obtained from Tokyo Chemical Industry (TCI) and were employed as such. PTAA (M_n = 5000-15000 by GPC) was procured from Xi´an Polymer Light Technology Corp.

Synthesis of 2D MoS_2: The intercalation of MoS_2 was carried out by stirring required amount of bulk MoS_2 in 5 ml of butyl lithium/hexane solution for 24 h and then ultra-sonicating for 2 h. Excess butyl lithium was washed out by dilution with hexane and filtration. The residual was dissolved in isopropanol and ultra-sonicated for 2 h and the resultant solution was centrifuged for 15 min to remove excess lithium ions by discarding the supernatant. This ultra-sonication and centrifugation processes were repeated two times and the final residual was collected and dissolve in isopropanol. The concentration of the final solution was adjusted to c.a 0.3 mg/ml by evaporation at room temperature.

Synthesis of SnO_2 QDs: SnO_2 QDs were synthesized according to the reported method.[68] In short, 3:1 mass ratio of $SnCl_2.2H_2O$ and CH_4N_2S were dissolved in 30 ml of deionized water under vigorous stirring for 48 h at room temperature to obtain a clear yellow colour solution. The obtained SnO_2 QD solution was filtered three times using 0.45 μm PTFE filter prior to use.

Device fabrication: The laser etched FTO-coated glasses (NSG10) were subsequently ultra-sonicated with Hellmanex II solution for 30 min and washed with deionized water and ethanol followed by ultra-sonication in acetone, ethanol and isopropanol for 20 min each step and dried using compressed air. All

the substrates were further treated by UV-ozone for 30 min prior to use. TiO_2 compact layer was then deposited using spray pyrolysis at 500 ºC employing 1mL of titanium diisopropoxide bis(acetyl acetonate) precursor solution (75 % in 2-propanol) in 19 mL of pure ethanol using oxygen as carrier gas and substrates were kept for another 30 minutes at 500 ºC to acquire anatase phase. After the films cooled down to room temperature, the resultant electrodes were treated by UV-ozone for another 30 min. The electron transport layer was spin coated atop of TiO_2 compact layer, by using SnO_2 QD solution followed by annealing on a hot plate progressively to 200 ºC for 1 h in air. After cooling down to room temperature the samples were treated by UV-ozone for 15 min and transferred to the Argon-filled glovebox under controlled moisture and oxygen conditions (H_2O level: <1 ppm and O_2 level: <10 ppm). Triple-cation perovskite precursor solution was prepared containing CsI (0.10 M), FAI (1.05 M), PbI_2 (1.24 M), MABr (0.12M) and $PbBr_2$ (0.12 M) in an anhydrous solvent mixture of *N*,*N*-dimethylformamide (DMF) and dimethylsulfoxide (DMSO) with 4:1 volume ratio. The perovskite precursor solution was then spin coated in a two-step spin-coating program set at 1000 rpm and 6000 rpm for 10 and 30 s, respectively where 112 µL chlorobenzene was dripped at 10 s before ending the program. Then the films were annealed at 100 ºC for 1 h for perovskite crystallization. After cooling down to room temperature 0.3 mg/ml MoS_2 in isopropanol solution was spin coated at 2000 rpm for 30 s. The hole transport layer was deposited through spin coating of pristine PTAA solution in toluene (3000 rpm for 35 s). For control devices, PTAA was directly deposited on perovskite active layer. The devices were finished by evaporating Au (80 nm, <1 Å/s) in an thermal evaporator under low vacuum conditions (10^{-7} Torr).

Materials characterization: X-ray photoelectron spectroscopy (XPS) experiments were carried out on a SPECS system (Berlin, Germany) equipped with Phoibos 150 1D-DLD analyzer with monochromated Al K_α radiation (1486.7 eV). The wide scan was performed with the step energy of 1 eV (dwell time: 0.1 s, pass energy: 80 eV), and detailed analysis of the elements was performed using 0.08 eV step energy (dwell time: 0.1 s, pass energy: 30 eV) with an electron exit angle of 90º. The spectra was adjusted using CasaXPS 2.3.16 software, which models Gauss-Lorentzian contributions. Atomic Force Microscopy (AFM) images were acquired with CSI Nano observer AFM and data were analyzed using Gwyddion software. (The dispersion of 2D-MoS_2 was diluted 1:10 in IPA for AFM, 25 µl of the dilution was drop-cast onto SiO_2 wafer and dried at room temperature). The absorption spectra and PL steady-state measurements were acquired with the help of UV–vis–IR spectrophotometer (Varian Cary 50 UV/Vis Spectrophotometer) and a fluorescence spectrophotometer (PerkinElmer Instrument LS55) respectively. Cross and top-view microstructure were acquired by a Hitachi S-4800 scanning electron microscope.

Device Characterization: Current density-voltage (*J-V*) curves were performed using an Oriel solar simulator (Newport) producing 1 sun AM1.5G (1000 Wm^{-2}) 3A sunlight. The generated photocurrent was recorded at scan rate of 10 mV/s (pre-sweep delay: 10s) with the help of Keithley 2604 source meter and black metal mask (0.09 cm^2) was used over the active area of the device. IPCE measurements

were recorded using a 150 W xenon lamp attached to a Bentham PVE300 motorized 1/4m monochromator. Temperature dependent capacitance-frequency measurements were performed with LCR meter model No. E4980A along with a Linkam (LTS420) sample heating control system filled with nitrogen in a closed environment.

Supporting Information

Supplemental information includes Figure S1-S11, and can be found with this article online or from the authors.

Acknowledgements

This work has received funding from the European Union H2020 Programme under European Research council Consolidator grant [MOLEMAT, 726360] and PARASOL (RTI2018-102292-B-I00) from Spanish ministry of Science and Innovation. We gratefully acknowledge Advanced Research Facilities (SGIker) of the University of Basque Country / Euskal Herriko Unibertsitatea and David Payno for help with LabVIEW programme.

Conflict of Interest

The authors declare no conflict of interest.

References

[1] A. Kojima, K. Teshima, Y. Shirai, T. Miyasaka, J. Am. Chem. Soc. 131 (2009) 6050-6051.

[2] "NREL Efficiency Chart. http://www.nrel.gov/ncpv/images/efficiency_chart.jpg," n.d.

[3] L.-L. Jiang, Z.-K. Wang, M. Li, C.-H. Li, P.-F. Fang, L.-S. Liao, J. Mater. Chem. A. 7 (2019) 3655-3663.

[4] J. Luo, J. Xia, H. Yang, L. Chen, Z. Wan, F. Han, H. A. Malik, X. Zhu, C. Jia, Energy Environ. Sci. 11 (2018) 2035-2045.

[5] X. Zheng, Y. Hou, C. Bao, J. Yin, F. Yuan, Z. Huang, K. Song, J. Liu, J. Troughton, N. Gasparini, C. Zhou, Y. Lin, D.-J. Xue, B. Chen, A. K. Johnston, N. Wei, M. N. Hedhili, M. Wei, A. Y. Alsalloum, P. Maity, B. Turedi, C. Yang, D. Baran, T. D. Anthopoulos, Y. Han, Z.-H. Lu, O. F. Mohammed, F. Gao, E. H. Sargent, O. M. Bakr, Nat. Energy 5 (2020) 131-140.

[6] X. Liu, Y. Cheng, B. Tang, Z. G. Yu, M. Li, F. Lin, S. Zhang, Y.-W. Zhang, J. Ouyang, H. Gong, Nano Energy 71 (2020) 104556.

[7] M. Chen, M.-G. Ju, H. F. Garces, A. D. Carl, L. K. Ono, Z. Hawash, Y. Zhang, T. Shen, Y. Qi, R. L. Grimm, D. Pacifici, X. C. Zeng, Y. Zhou, N. P. Padture, Nat. Commun. 16 (2019).

[8] Y. Liu, Z. Liu, E.-C. Lee, ACS Appl. Energy Mater. 2(2019) 1932-1942.

[9] Q. Wang, N. Phung, D. D. Girolamo, P. Vivo, A. Abate, Energy Environ. Sci. 12 (2018) 865-886.

[10] X. Liu, T. J. Huang, L. Zhang, B. Tang, N. Zhang, D. Shi, H. Gong, Chem. Eur. 24 (2018) 4991-4998.
[11] N. Arora, M. I. Dar, A. Hinderhofer, N. Pellet, F. Schreiber, S. M. Zakeeruddin, M. Grätzel, Science. 358 (2017) 768-771.
[12] N. Ahn, K. Kwak, M. S. Jang, H. Yoon, B. Y. Lee, J.-K. Lee, P. V. Pikhitsa, J. Byun, M. Choi, Nat. Commun. 7 (2016).
[13] G. Kakavelakis, I. Paradisanos, B. Paci, A. Generosi, M. Papachatzakis, T. Maksudov, L. Najafi, A. E. D. R. Castillo, G. Kioseoglou, E. Stratakis, F. Bonaccorso, E. Kymakis, Adv. Energy Mater. 8 (2018) 1702287.
[14] S. Tsarev, I. K. Yakushchenko, S. Y. Luchkin, P. M. Kuznetsov, R. S. Timerbulatov, N. N. Dremova, L. A. Frolova, K. J. Stevenson, P. A. Troshin, Sustain. Energ. Fuels. 3 (2019) 2627-2632.
[15] R. Singh, A. Giri, M. Pal, K. Thiyagarajan, J. Kwak, J.-J. Lee, U. Jeong, K. Cho, J. Mater. Chem. A. 7 (2019) 7151-7158.
[16] P. Huang, Z. Wang, Y. Liu, K. Zhang, L. Yuan, Y. Zhou, B. Song, Y. Li, ACS Appl. Mater. Interfaces 9 (2017) 25323-25331.
[17] D. H. Shin, J. S. Ko, S. K. Kang, S.-H. Choi, ACS Appl. Mater. Interfaces. 12 (2020) 4586-4593.
[18] X. Yang, W. Fu, W. Liu, J. Hong, Y. Cai, C. Jin, M. Xu, H. Wang, D. Yang, H. Chen, J. Mater. Chem. A. 2 (2014) 14798-14806.
[19] J. Kopaczek, M. P. Polak, P. Scharoch, K. Wu, B. Chen, S. Tongay, R. Kudrawiec, J. Appl. Phys. 119 (2016) 235705.
[20] E. Singh, K. S. Kim, G. Y. Yeom, H. S. Nalwa, ACS Appl. Mater. Interfaces. 9 (2017) 3223-3245.
[21] B. Zheng, Y. Chen, Iop Conf. Ser. Mater. Sci. Eng. 274 (2017) 012085.
[22] A. M. V. D. Zande, P. Y. Huang, D. A. Chenet, T. C. Berkelbach, Y. You, G.-H. Lee, T. F. Heinz, D. R. Reichman, D. A. Muller, J. C. Hone, Nat. Mater. 12 (2013) 554-561.
[23] K. F. Mak, C. Lee, J. Hone, J. Shan, T. F. Heinz, PRL. 105 (2010) 136805.
[24] L. Najafi, B. Taheri, B. Martín-García, S. Bellani, D. D. Girolamo, A. Agresti, R. Oropesa-Nuñez, S. Pescetelli, L. Vesce, E. Calabrò, M. Prato, A. E. D. R. Castillo, A. D. Carlo, F. Bonaccorso, ACS Nano. 12 (2018) 10736-10754.
[25] C. Backes, N. C. Berner, X. Chen, P. Lafargue, P. LaPlace, M. Freeley, G. S. Duesberg, J. N. Coleman, A. R. McDonald, Angew. Chem. Int. Ed. Engl. 23 (2015) 2638-2642.
[26] Y. Cai, X. Yang, T. Liang, L. Dai, L. Ma, G. Huang, W. Chen, H. Chen, H. Su, M. Xu, Nanotechnology. 25 (2014) 465401.
[27] G. Eda, H. Yamaguchi, D. Voiry, T. Fujita, M. Chen, M. Chhowalla, Nano Lett. 12 (2011) 5111-5116.
[28] M. Abuhelaiqa, S. Paek, Y. Lee, K. T. Cho, S. Heo, E. Oveisi, A. J. Huckaba, H. Kanda, H. Kim, Y. Zhang, R. H. Baker, S. Kinge, A. M. Asiri, M. K. Nazeeruddin, Energy Environ. Sci. 12 (2019) 1910-1917.

[29] H. Guo, H. Zhang, J. Yang, H. Chen, Y. Li, L. Wang, X. Niu, ACS Appl. Energy Mater. 1 (2018) 6936-6944.
[30] J. K. Ellis, M. J. Lucero, G. E. Scuseria, Appl. Phys. Lett. 99 (2011) 261908.
[31] W. S. Yun, S. W. Han, S. C. Hong, I. G. Kim, J. D. Lee, Phys. Rev. B 85 (2012) 033305.
[32] C. H. Ng, T. S. Ripolles, K. Hamada, S. H. Teo, H. N. Lim, J. Bisquert, S. Hayase, Sci. Rep. 8 (2018) 2482.
[33] N. J. Jeon, H. G. Lee, Y. C. Kim, J. Seo, J. H. Noh, J. Lee, S. I. Seok, J. Am. Chem. Soc. 136 (2014) 7837-7840.
[34] H. S. Kim and N. G. Park, J. Phys. Chem. Lett. 5 (2014) 2927-2934.
[35] W. Wei, K. Sun, Y. H. Hu, J. Mater. Chem. A. 4 (2016) 12398-12401.
[36] F. Zhang, H. Lu, J. Tong, J. J. Berry, M. C. Beard, K. Zhu, Energy Environ. Sci. 13 (2020) 1154-1186.
[37] G. Wu, X. Li, J. Zhou, J. Zhang, X. Zhang, X. Leng, P. Wang, M. Chen, D. Zhang, K. Zhao, S. Liu, H. Zhou, Y. Zhang, Adv. Mater. 31 (2019) 1903889.
[38] F. Zhang, K. Zhu, Adv. Energy Mater. 10 (2020) 1902579- 1902605.
[39] L. Meng, C. Sun, R. Wang, W. Huang, Z. Zhao, P. Sun, T. Huang, J. Xue, J. W. Lee, C. Zhu, Y. Huang, Y. Li, Y. Yang, J. Am. Chem. Soc. 140 (2018) 17255-17262.
[40] J. Yang, S. Xiong, T. qu, Y. Zhang, X. He, X. Guo, Q. Zhao, S. Braun, J. Chen, J. Xu, Y. Li, X. Liu, C. Duan, J. Tang, M. Fahlman, Q. Bao, ACS Appl. Mater. Interfaces. 11 (2019) 13491-13498.
[41] Z. Liu, K. Liu, F. Zhang, S. M. Jain, T. He, Y. Jiang, P. Liu, J. Yang, H. Liu, M. Yuan, Solar Energy 195 (2020) 436-445.
[42] A. Agresti, S. Pescetelli, A. L. Palma, B. M. Garcia, L. Najafi, S. Bellani, I. Moreels, M. Prato, F. Bonaccorso, A. D. Carlo, ACS Energy Lett. 4 (2019) 1862-1871.
[43] B. Zhang, Y. Zhou, Q. Xue, J. Tian, Q. Yao, Y. Zang, L. Wang, W. Yang, H. L. Yip, Y. Cao, Solar RRL. 3 (2019) 1900265.
[44] J. Lee, P. Dak, Y. Lee, H. Park, W. Choi, M. A. Alam, S. Kim, Sci. Rep. 4 (2014) 07352
[45] J. H. Kim, T. J. Ko, E. Okogbue, S. S. Han, M. S. Shawkat, M. G. Kaium, K. H. Oh, H. S. Chung, Y. Jung, Sci. Rep. 9 (2019) 1641.
[46] S. Kelebek, J. Colloid Interface Sci. 124 (1988) 504-514.
[47] S. Zhang, X. Zeng, Z. Tang, M. Tan, Int. J. Mod. Phys B. 16 (2002) 1080-1085.
[48] Q. H. Wang, K. K. Zadeh, A. Kis, J. N. Coleman, M. S. Strano, Nature Nanotech. 7 (2012) 699-712
[49] A. P. Gaur, S. Sahoo, M. Ahmadi, S. P. Dash, M. J. Guinel, R. S. Katiyar, Nano Lett. 14 (2014) 4314-4321.
[50] I. Zarazua, J. Bisquert, G. Garcia-Belmonte, J. Phys. Chem. Lett. 7 (2016) 525-528.
[51] G. G. Belmonte, J. Bisquert, ACS Energy Lett. 1 (2016) 683-688.
[52] O. Almora, C. Aranda, G. Garcia-Belmonte, J. Phys. Chem. C 122 (2017) 13450-13454.

[53] O. Almora, A. Guerrero, G. Garcia-Belmonte, Appl. Phys. Lett. 108 (2016) 043903.
[54] R. A. Awni, Z. Song, C. Chen, C. Li, C. Wang, M. A. Razooqi, L. Chen, X. Wang, R. J. Ellingson, J. V. Li, Y. Yan, Joule 4 (2020) 644-657.
[55] H. Zang, Y. C. Hsiao, B. Hu, Phys.Chem.Chem.Phys. 16 (2014) 4971-4976.
[56] O. Almora, I. Zarazua, E. Mas-Marza, I. Mora-Sero, J. Bisquert, G. Garcia-Belmonte, J. Phys. Chem. Lett. 6 (2015) 1645-1652.
[57] M. T. Khan, A. R. D. Almohammedi, S. Kazim, S. Ahmad, *Chem. Rec.* 20 (2020) 452-465.
[58] M. Samiee, S. Konduri, B. Ganapathy, R. Kottokkaran, H. A. Abbas, A. Kitahara, P. Joshi, L. Zhang, M. Noack, V. Dalal, Appl. Phys. Lett. 105 (2014) 153502.
[59] J. A. Carr, M. Elshobaki, S. Chaudhary, Appl. Phys. Lett. 107 (2015) 203302.
[60] H. Jin, E. Debroye, M. Keshavarz, I. G. Scheblykin, M. B. J. Roeffaers, J. Hofkens, J. A. Steele, Mater. Horiz. 7 (2020) 397-410.
[61] N. H. Hemasiri, S. Kazim, L. Calio, S. Paek, M. Salado, G. Pozzi, L. Lezama, M. K. Nazeeruddin, S. Ahmad, ACS Appl. Mater. Interfaces. 12 (2020) 9395-9403.
[62] K. Gelderman, L. Lee, S. W. Donne, J. Chem. Educ. 84 (2007) 685-688.
[63] A. Guerrero, E. J. Juarez-Perez, J. Bisquert, I. Mora-Sero, G. Garcia-Belmonte, Appl. Phys. Lett. 105 (2014) 133902.
[64] S. Aharon, S. Gamliel, B. E. Cohen, L. Etgar, Phys.Chem.Chem.Phys. 16 (2014) 10512-10518.
[65] T. Bu, X. Liu, Y. Zhor, J. Yi, X. Huang, L. Luo, J. Xiao, Z. Ku, Y. Peng, F. Huang, Y. B. Cheng, J. Zhong, Energy Environ. Sci. 10 (2017) 2509-2515.
[66] Y. Shao, Z. Xiao, C. Bi, Y. Yuan, J. Huang, Nat Commun. 5 (2014) 5784.
[67] J. A. Carr, S. Chaudhary, Energy Environ. Sci. 6 (2013) 3414-3438.
[68] G. Yang, C. Chen, F. Yao, Z. Chen, Q. Zhang, X. Zheng, J. Ma, H. Lei, P. Qin, L. Xiong, W. Ke, G. Li, Y. Yan, G. Fang, Adv. Mater. 30 (2018) 1706023.

Supporting Information

Reduced trap density and mitigating the interfacial losses by placement of 2D dichalcogenide material at perovskite/HTM interface in a dopant free perovskite solar cells

Naveen Harindu Hemasiri[1], Samrana Kazim[1,2] and Shahzada Ahmad[1,2]

[1]BCMaterials, Basque Center for Materials, Applications and Nanostructures, Bld. Martina Casiano, UPV/EHU Science Park, Barrio Sarriena s/n, 48940 Leioa, Spain

Tel: +34 946128811 Email:shahzada.ahmad@bcmaterials.net

[2]IKERBASQUE, Basque Foundation for Science, Bilbao, 48013, Spain

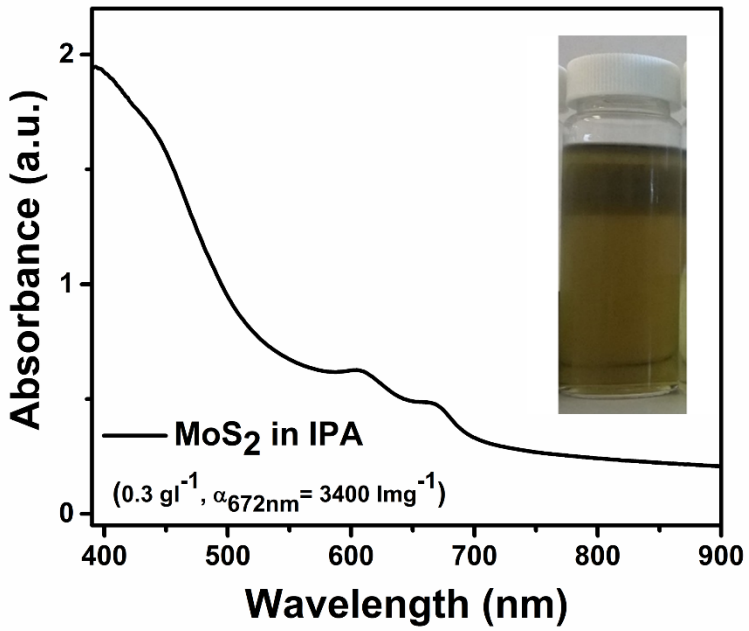

Figure S1. UV-Vis absorption spectrum of 2D-MoS_2 solution. Insert shows the stable solution of 2D-MoS_2 in isopropanol (IPA)

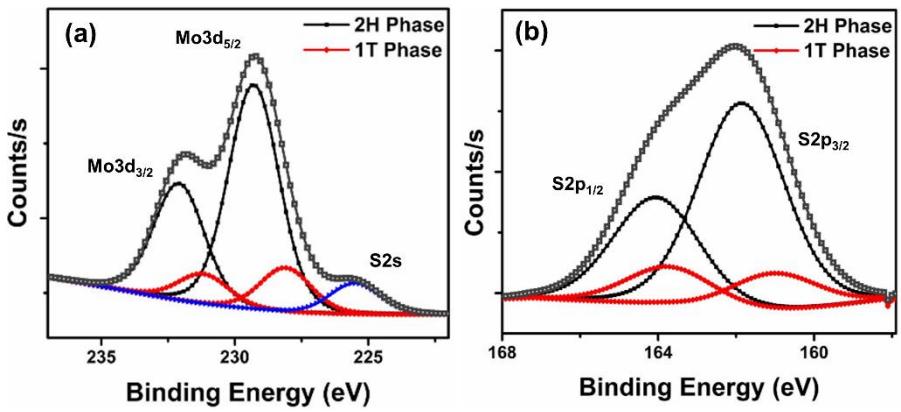

Figure S2. XPS narrow spectrum of (a) Mo3d and (b) S2p of spin coated MoS_2 (synthesized via liquid exfoliation with the absence of lithium intercalation) thin film. Black and red plots respectively represent the 2H and 1T contributions.

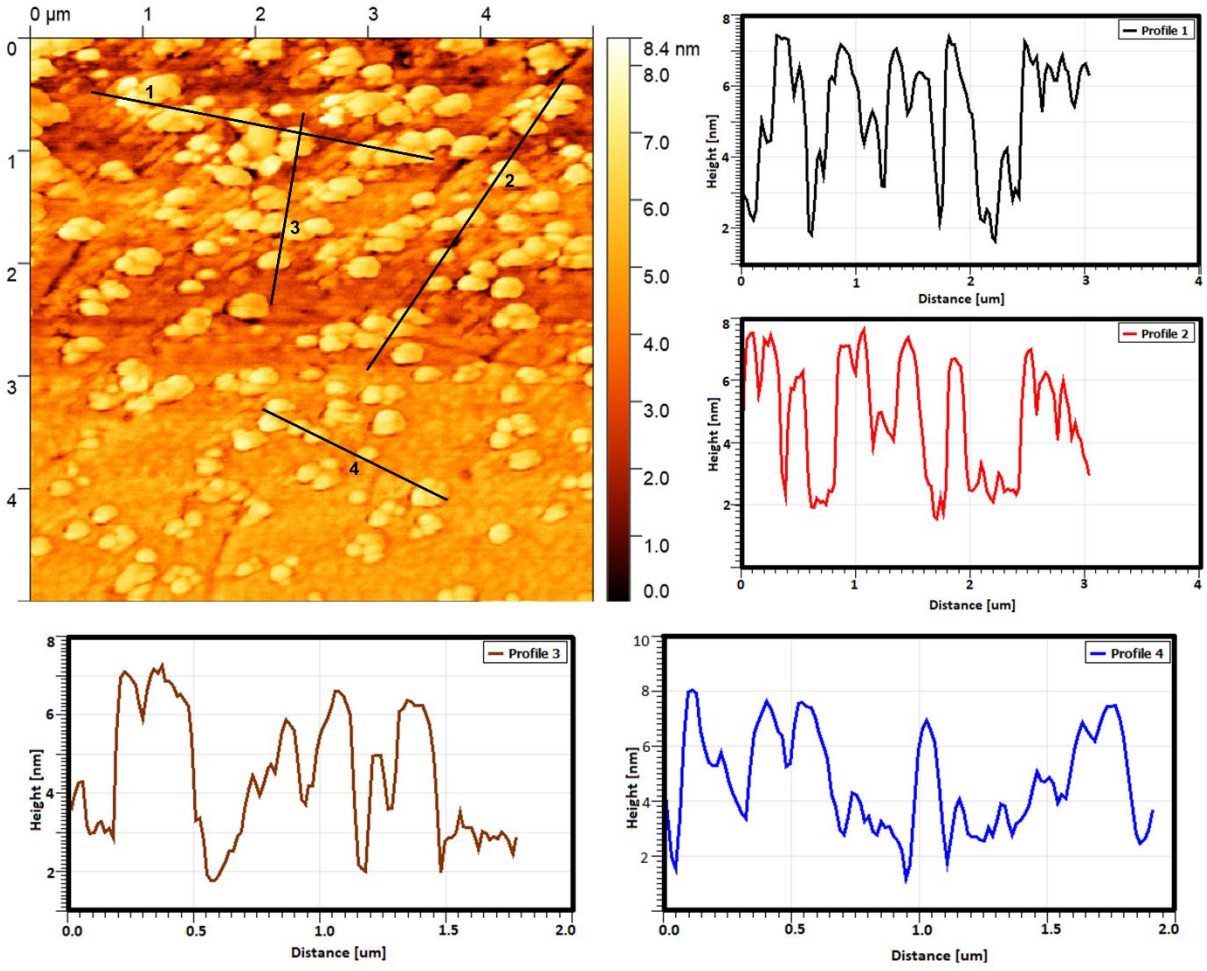

Figure S3. AFM height image of 2D-MoS_2 on SiO_2 substrate and thickness profiles.

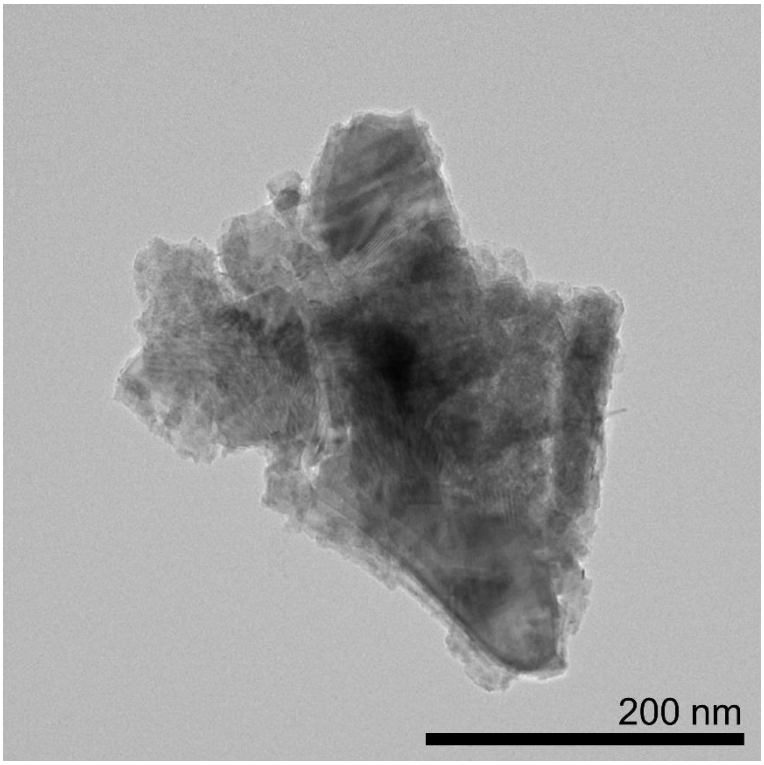

Figure S4. Transmission electron microscopy (TEM) of 2D-MoS_2 drop-casted on Cu grid.

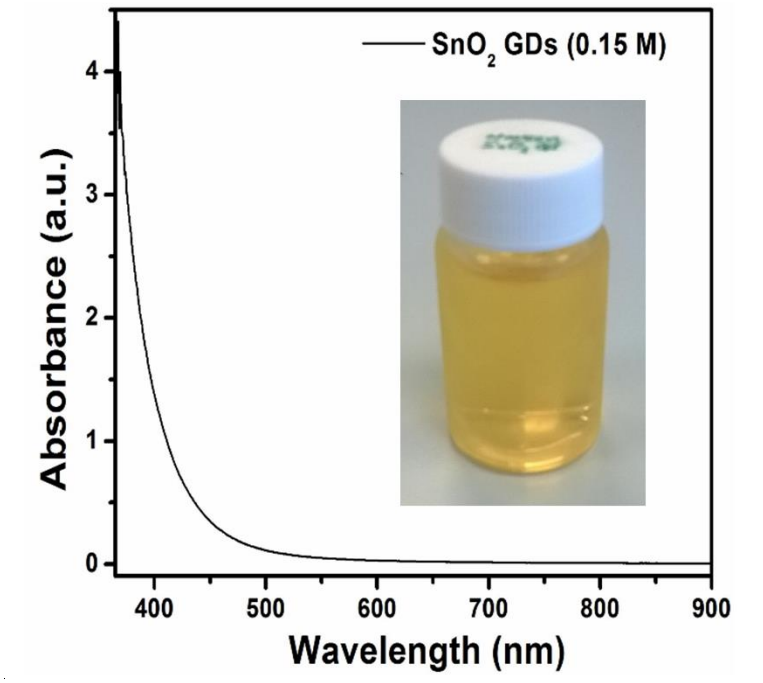

Figure S5. UV-Vis absorption spectrum of aqueous SnO_2 QDs solution. Insert shows the stable solution of SnO_2 QDs.

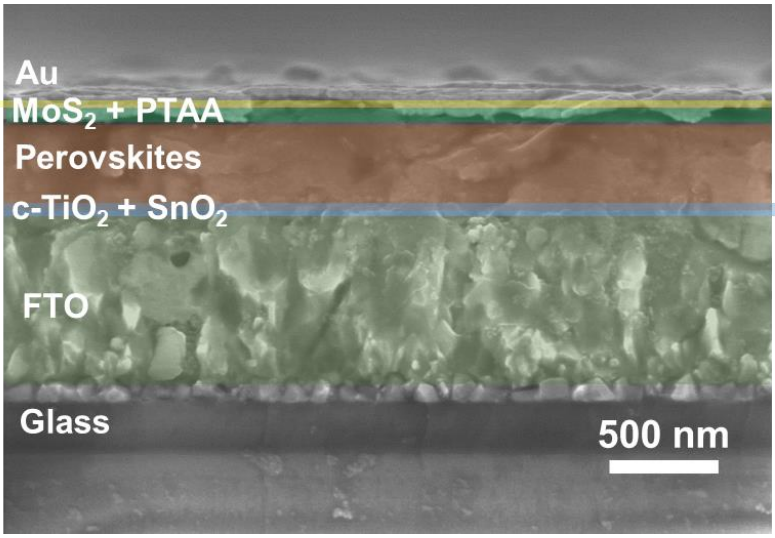

Figure S6. Cross sectional SEM image of the device with 2D-MoS_2 as interfacial layer.

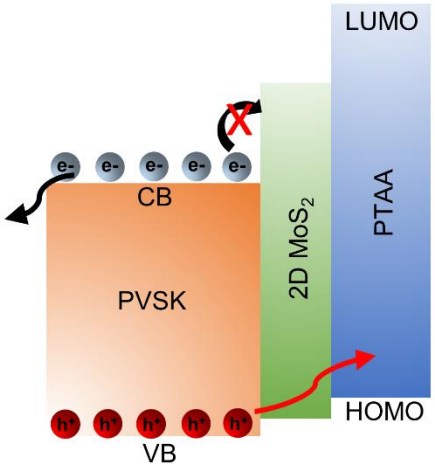

Figure S7. Electron blocking at the CsFAMA and PTAA interface due to presence of 2D-MoS_2 interface layer.

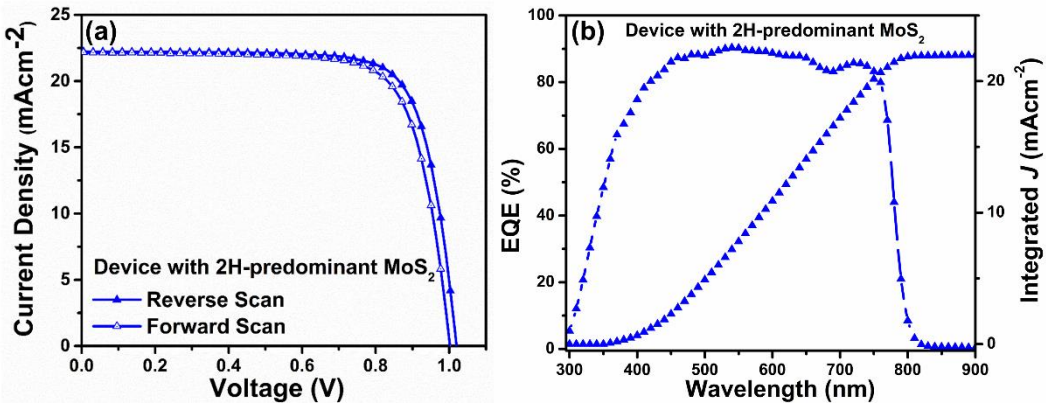

Figure S8. (a) *J-V* hysteresis curve and (b) corresponding IPCE and integrated current for the device with 2H-predominant 2D-MoS_2 as an interfacial layer.

Table S1. Average photovoltaic performance of control and modified devices.

Device	V_{oc} (V)	J_{sc} (mAcm^{-2})	FF	PCE (%)
Control	0.887 ± 0.009	22.49 ± 0.18	73.28 ± 0.8	14.65 ± 0.16
Modified	1.04 ± 0.017	22.07 ± 0.11	79.13 ± 0.9	18.17 ± 0.18

Table S2. Device statistics of control device.

Device No.	V_{oc} (V)	J_{sc} (mAcm^{-2})	FF (%)	PCE (%)
01	0.899	22.29	71.53	14.33
02	0.883	22.68	74.01	14.83
03	0.899	22.30	72.85	14.60
04	0.905	22.46	71.75	14.58
05	0.849	22.62	72.01	14.55
06	0.885	22.52	73.54	14.65
07	0.884	22.34	72.66	14.37
08	0.887	22.70	74.64	15.04
09	0.898	22.07	73.93	14.66
10	0.872	22.65	73.61	14.53

Table S2. Device statistics of modified device (with 2D-MoS_2).

Device No.	V_{oc} (V)	J_{sc} (mAcm^{-2})	FF (%)	PCE (%)
01	1.011	22.19	79.75	17.89
02	1.047	21.97	79.43	18.27
03	1.049	21.99	79.26	18.29
04	1.006	22.23	79.67	17.82
05	1.063	22.02	77.61	18.16
06	1.032	21.99	80.11	18.18
07	1.029	22.05	79.79	18.09
08	1.053	22.02	79.96	18.53
09	1.055	21.98	77.94	18.07
10	1.059	22.27	77.73	18.33

Table S3. Statistics of PV parameters for devices with 2H-predominant 2D-MoS_2 as an interfacial layer.

Device	V_{oc} (mV)	J_{sc} (mAcm^{-2})	FF (%)	PCE (%)
01	1013.6	22.20	76.39	17.19
02	1041.6	22.25	72.81	16.87
03	1013.7	22.18	76.41	17.18
04	1018.7	22.22	76.61	17.35
05	1039.6	22.22	73.89	17.07
Average	1025.4±12.534	22.21±0.0248	75.22±1.569	17.13±0.156

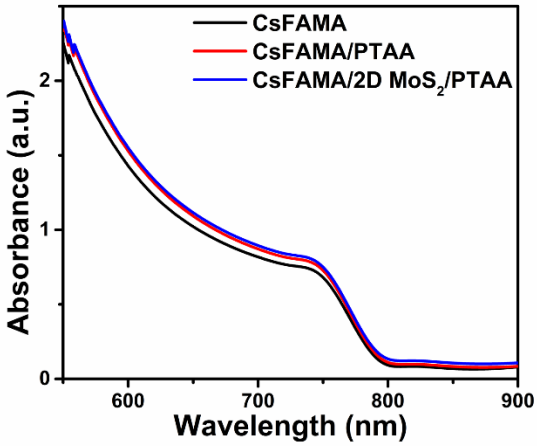

Figure S9. UV-Vis absorption spectra of CsFAMA, CsFAMA/PTAA and CsFAMA/2D MoS_2/PTAA.

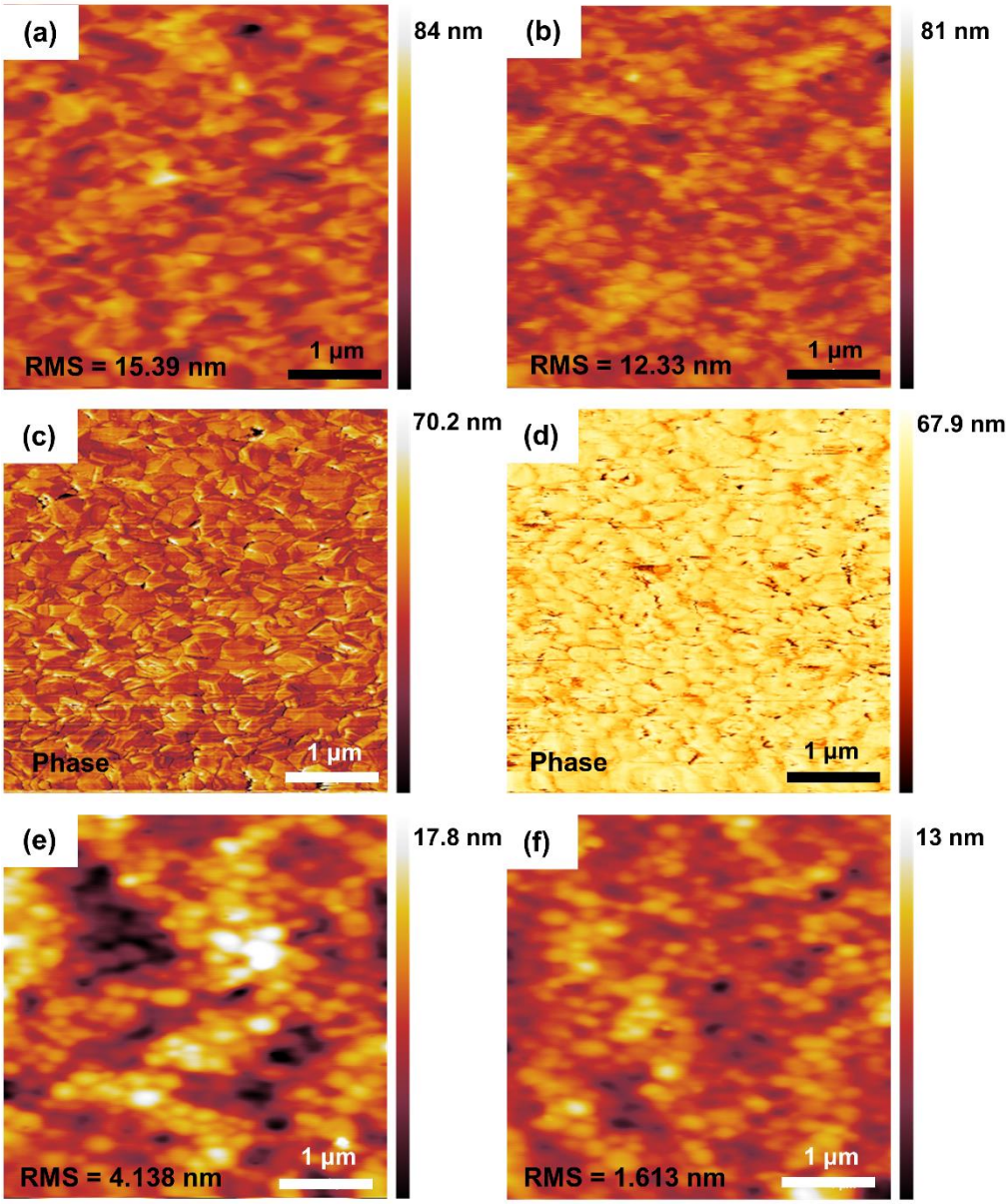

Figure S10: AFM topography images of (a) CsFAMA, (b) 2D-MoS_2/CsFAMA, and phase images of (c) CsFAMA, (d) 2D-MoS_2/CsFAMA film, (e) PTAA on CsFAMA film and (f) PTAA on 2D-MoS_2/CsFAMA.

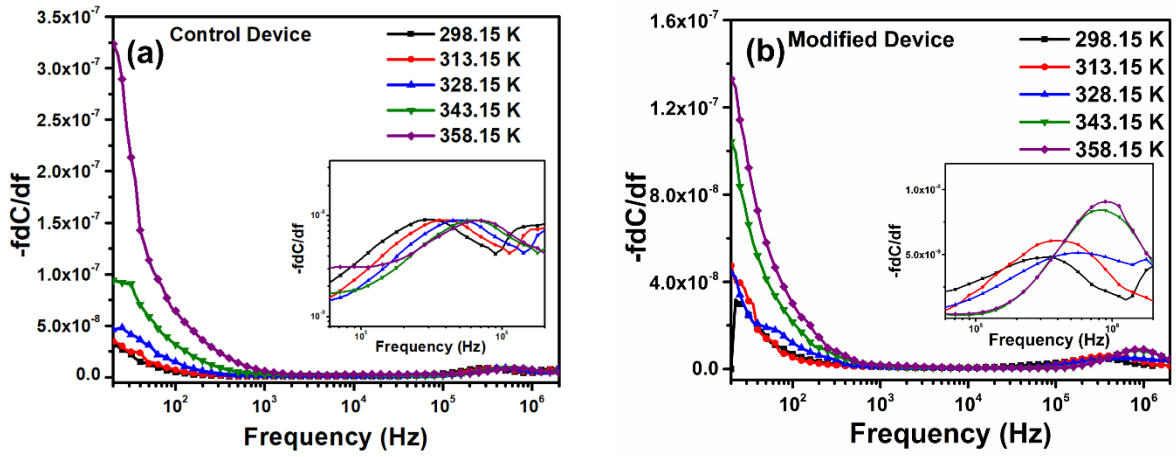

Figure S11. *–f dC/df* versus frequency at variable temperature for (a) control and (b) modified devices.